

Orbital doublet driven even-spin Chern insulators

Lu Liu,^{1,2,*} Yuntian Liu,^{1,*} Jiayu Li,¹ Hua Wu,^{2,3,4,†} and Qihang Liu^{1,5,‡}

¹*Department of Physics and Shenzhen Institute for Quantum Science and Engineering (SIQSE), Southern University of Science and Technology, Shenzhen 518055, China*

²*Laboratory for Computational Physical Sciences (MOE), State Key Laboratory of Surface Physics, and Department of Physics, Fudan University, Shanghai 200433, China*

³*Shanghai Qi Zhi Institute, Shanghai 200232, China*

⁴*Collaborative Innovation Center of Advanced Microstructures, Nanjing 210093, China*

⁵*Guangdong Provincial Key Laboratory of Computational Science and Material Design, Southern University of Science and Technology, Shenzhen 518055, China*

(Dated: August 2, 2024)

Quantum spin Hall insulators hosting edge spin currents hold great potential for low-power spintronic devices. In this paper, we present a universal approach to achieve a high and near-quantized spin Hall conductance plateau within a sizable bulk gap. Using a nonmagnetic four-band model Hamiltonian, we demonstrate that an even-spin Chern (ESC) insulator can be accessed by tuning the sign of spin-orbit coupling (SOC) within a crystal symmetry-enforced orbital doublet. With the assistance of a high spin Chern number of $C_S = -2$ and spin $U(1)$ quasisymmetry, this orbital-doublet-driven ESC phase is endowed with the near-double-quantized spin Hall conductance. We identify 12 crystallographic point groups supporting such a sign-tunable SOC. Furthermore, we apply our theory to realistic examples, and show the phase transition from a trivial insulator governed by positive SOC in the RuI_3 monolayer to an ESC insulator dominated by negative SOC in the RuBr_3 monolayer. This orbital-doublet-driven ESC insulator, RuBr_3 , showcases nontrivial characteristics including helical edge states, near-double-quantized spin Hall conductance, and robust corner states. Our work provides different pathways in the pursuit of the long-sought quantum spin Hall insulators.

INTRODUCTION

Two-dimensional (2D) quantum spin Hall (QSH) insulators have garnered significant interest for their promising applications in spintronics and magnetoelectronics [1–4]. They manifest topologically protected helical edge states where the spin is locked to the momentum through spin-orbit coupling (SOC) and time-reversal symmetry (TRS), providing dissipationless spin transports ideal for low-power magnetic memory devices. The first predictions of realistic QSH insulators identified graphene [1] and the HgTe quantum well [2] as candidates, each characterized by a SOC-induced inverted bulk gap along with a pair of helical edge states within this gap. This topological phase is generally characterized by the topological invariant $Z_2 = 1$, which also serves as the symmetry indicator for TRS-preserved systems [5]. Over the years, this $Z_2 = 1$ topological phase has been observed in several quantum wells [6–8] and pristine 2D materials such as WTe_2 , bismuthene, Na_3Bi , and germanene [9–14].

In addition to the Z_2 index, the spin Chern number C_S , also established as a topological invariant, is directly related to the number of pairs of helical edge states [15]. In particular, when the real-spin component S_z remains preserved, C_S defines the quantized spin Hall conductance (SHC) as $\sigma_{xy}^S = C_S \frac{e}{2\pi}$. These two invariants are related by $Z_2 = \text{mod}(C_S, 2)$. Therefore, QSH insulators with two pairs of helical edge states in the $|C_S| = 2$

regime are considered to be trivial within conventional Z_2 classification. However, experiments have observed near-double-quantized conductance in twisted bilayers WSe_2 and MoTe_2 [16, 17], demonstrating that QSH effects can indeed manifest in even-spin Chern (ESC) insulators. Regarding the absence of spin $U(1)$ symmetry in realistic materials and the consequent lack of exact quantization of SHC [5, 15, 18], we have recently emphasized the pivotal role of spin $U(1)$ quasisymmetry for the near-quantization of SHC in TRS-preserved $Z_2 = 1$ or such $Z_2 = 0$ systems, as well as TRS-broken cases [19]. Beyond theoretical predictions of magnetic high spin Chern insulators [20], and the ESC phase in monolayer α - Sb/Bi [21–23] and magnetic Fe_2BrMgP monolayer and TiTe bilayer [24], we have predicted near-double-quantized SHC in twisted bilayer transition metal dichalcogenides and monolayer RuBr_3 [19] protected by spin $U(1)$ quasisymmetry. In this paper, we will present a general approach to realize an ESC phase with a symmetry-protected near-double-quantized SHC within a large bulk gap, which would be an ideal platform for observing QSH effects and further promote applications of QSH insulators.

First, using a nonmagnetic four-band model Hamiltonian, we demonstrate that an ESC phase with $C_S = -2$ can be accessed by tuning the sign of SOC within a crystal symmetry-enforced orbital doublet, as shown in Fig. 1. Such an orbital-doublet-driven ESC phase is endowed with two notable features: (i) a sizable bulk gap opened by first-order spin-preserved SOC; (ii) a high near-quantized SHC approaching -2 (in unit of $e/2\pi$) protected by spin $U(1)$ quasisymmetry. Thereafter, we enumerate 12 crystallographic point groups supporting the orbital doublets with sign-alterable SOC effects. Fur-

* Lu Liu and Yuntian Liu contributed equally to this work.

† Corresponding author. wuh@fudan.edu.cn

‡ Corresponding author. liuqh@sustech.edu.cn

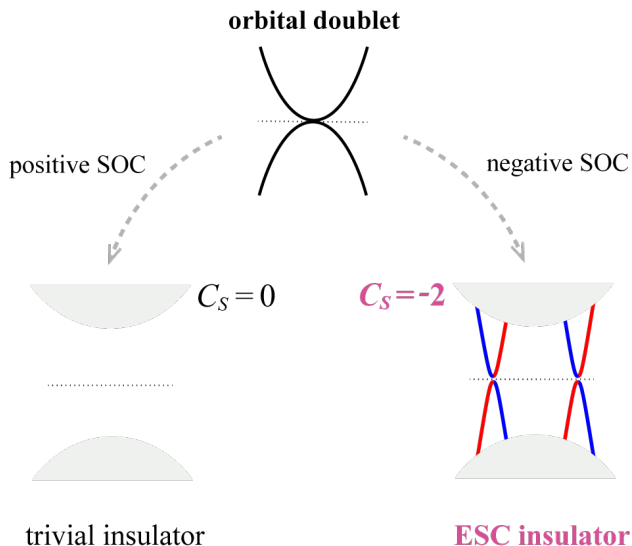


FIG. 1. Schematic for designing ESC insulators with $C_S = -2$: by tuning the sign of SOC within an orbital doublet from positive to negative, a phase transition from $C_S = 0$ to $C_S = -2$ can be realized.

thermore, we present realistic examples to demonstrate our theory. As shown below, a trivial insulator driven by positive SOC transforms into a nontrivial ESC insulator induced by negative SOC, as observed in the transition from monolayer RuI₃ to RuBr₃. In addition to the topologically nontrivial features such as the near-double-quantized SHC and two pairs of helical edge states, we further show robust in-gap corner states that is associated with the slightly gapped edge states in RuBr₃.

COMPUTATIONAL DETAILS

Density functional theory calculations are performed using the full-potential augmented plane wave plus the local orbital code (Wien2k) [25]. The optimized lattice constants of RuI₃, RuBr₃, RuCl₃, and RuF₃ monolayers are $a = b = 6.667, 6.159, 5.747,$ and 4.827 Å, respectively. A vacuum slab of 15 Å is set along the c axis for both systems. The muffin-tin sphere radii are chosen to be 2.2, 2.4, 2.1, and 1.5 bohrs for Ru, I/Br, Cl, and F atoms, respectively. The cutoff energy of 14 Ry is set for plane wave expansions of interstitial wave functions. We use the $11 \times 11 \times 1$ k -mesh for integration over the Brillouin zone. SOC is included by the second variational method with scalar relativistic wave functions. Electron correlation of Ru $4d$ electrons is taken into account by adopting a typical Hubbard U of 2 eV and a Hund's exchange of 0.5 eV [26]. The Wannier functions of Ru $4d$, I $5p$, and Br $4p$ orbitals are constructed using Wien2wannier [27] and WANNIER90 [28] without performing maximally localized procedures. The topological edge states and SHC are calculated by the iterative Green's function and the Kubo formula [29], respectively, as implemented in WannierTools package [30]. Since the RuCl₃ monolayer exhibits

electronic structures and topological characters similar to those of RuBr₃, and the metallic RuF₃ monolayer is beyond our interests, we present the results for RuI₃ and RuBr₃ monolayers in the main text, and those for RuCl₃ and RuF₃ monolayers in Fig. 7 in the Appendix B.

RESULTS

I. Symmetry and model of even spin Chern phase

To begin with, we will show that a nontrivial ESC phase can be realized within a nonmagnetic four-band model Hamiltonian based on an orbital doublet that is characterized by a 2D irreducible representation (irrep). We consider a typical doublet formed by p_x and p_y orbitals as $p_{\pm} = (p_x \pm ip_y)/\sqrt{2}$, where the subscript $+/-$ denotes orbital angular momentum $l_z = +1/-1$. To generate a 2D irrep furnished by the p_{\pm} doublet, here we consider a D_{6h} point group, of which the generators are three-fold rotation symmetry C_{3z} along the z axis, two-fold rotation symmetry C_{2z}/C_{2y} along the z/y axis, and space inversion symmetry I . In the basis of $\{|p_+, \uparrow\rangle, |p_-, \uparrow\rangle, |p_+, \downarrow\rangle, |p_-, \downarrow\rangle\}$, the representation of symmetry operations is given by $C_{3z} = e^{i\frac{\pi}{3}\sigma_z} \otimes e^{i\frac{2\pi}{3}\tau_z}$, $C_{2z} = e^{i\frac{\pi}{2}\sigma_z} \otimes -\tau_0$, $C_{2y} = e^{i\frac{\pi}{2}\sigma_y} \otimes -\tau_x$, $I = \mathbb{I}_{2 \times 2} \otimes -\mathbb{I}_{2 \times 2}$, and TRS $T = \mathcal{K} \cdot i\sigma_y \otimes \tau_x$, where \mathcal{K} is the complex conjugation operator, $\mathbb{I}_{2 \times 2}$ is a 2×2 identity matrix, and $\sigma_{x,y,z}$ and $\tau_{x,y,z}$ are Pauli matrices for spin and orbital degrees of freedom, respectively. By imposing those symmetries, we derive the generic form of the effective Hamiltonian as follows:

$$H(\mathbf{k}) = \epsilon_0(\mathbf{k})\mathbb{I}_{4 \times 4} + C[(k_x^2 - k_y^2)\sigma_0 \otimes \tau_x + 2k_x k_y \sigma_0 \otimes \tau_y] + D(k_x^2 + k_y^2)\sigma_z \otimes \tau_z + E\sigma_z \otimes \tau_z \quad (1)$$

with $\epsilon_0(\mathbf{k}) = A - B(k_x^2 + k_y^2)$. Note that the symmetry preserves the term $E\sigma_z \otimes \tau_z$ which is contributed by the first-order spin-preserved SOC. The resulting electronic structure consists of two sets of doubly degenerate bands protected by I and T symmetry, yielding an energy gap $2E$. This bulk gap $2E$, primarily opened by first-order SOC, can reach ~ 100 meV to against thermal fluctuation and local disorder. Furthermore, the change of the sign of E from positive to negative marks a phase transition accompanied by band inversion, as shown in Fig. 2. Note that such band inversion does not change the Z_2 index of the system because the wavefunctions of the lowest conduction band and the highest valence band at Γ share the same parity. However, we find that such a band inversion signifies a topological phase transition from a trivial insulator to a nontrivial ESC insulator characterized by $C_S = -2$ (see Appendix A).

We note that such a topological phase transition, driven by altering the sign of the SOC within orbital doublets, can be achieved by orbital engineering. Specifically, some d -orbital doublets, undergoing transformations identical to the p_{\pm} doublet but with an opposite l_z , can contribute negative SOC in contrast to the pos-

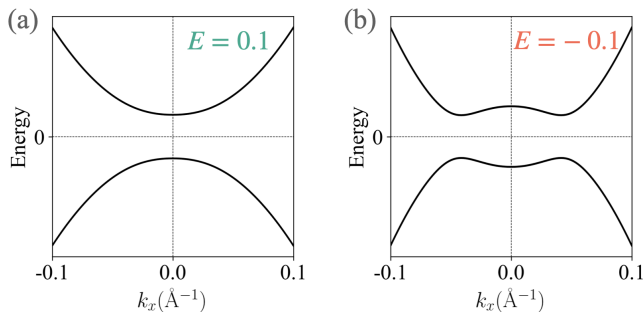


FIG. 2. Band structures of the model Hamiltonian in Eq. (1) with the parameters $A = B = 0, C = D = 0.3$: from (a) $E = 0.1$ to (b) $E = -0.1$, the band inversion marks a phase transition from a trivial insulator to an ESC insulator with $C_S = -2$.

itive one within p_{\pm} . We identify 12 crystallographic point groups that can support the sign-alterable SOC within specific orbital doublets, as listed in Table I. For instance, the orbital doublet $d_{\pm 2} = |l_z = \pm 2\rangle$ is supported by $(C_{3h}, D_{3h}, C_6, C_{6v}, C_{6h}, D_6, D_{6h})$ point groups. Under the rotational symmetries that can distinguish the two states in an orbital doublet, the d_{-2} state transform as p_+ , and d_{+2} transforms as p_- , e.g., the symmetry operation C_{3z} introduces a phase factor $e^{-i\frac{2\pi}{3}\tau_z}$ to $d_{\pm 2}$ but an opposite phase factor $e^{i\frac{2\pi}{3}\tau_z}$ to p_{\pm} . Therefore, the $d_{\pm 2}$ doublet will yield a negative splitting when SOC emerges, in contrast to the positive SOC-splitting in p_{\pm} . Similarly, the e'_{\pm} doublet supported by $(C_3, C_{3v}, D_3, D_{3d}, S_6)$ point groups is formulated as $e'_{\pm} = \pm \cos\alpha |l_z = \pm 2\rangle - \sin\alpha |l_z = \mp 1\rangle$, where $\sin^2\alpha$ varies from 0 to 1/3 depending on local d -orbital environments [31]. The e'_{\pm} transforms as p_{\mp} , and thus also provides a negative SOC. Note that two other d -orbital doublets listed in Table I, specifically $d_{\pm} = |l_z = \pm 1\rangle$ and $e'_{g\pm} = \sin\alpha |l_z = \mp 2\rangle \mp \cos\alpha |l_z = \pm 1\rangle$, both yield the positive SOC just as that in p_{\pm} .

We emphasize that among the 12 crystallographic point groups in Table I, while lowering symmetries from the highest symmetric point group D_{6h} [Eq. (1)] may introduce additional terms, the low-energy physics at the Γ point remains intact. For instance, in point group D_{3d} , the term $F[(k_x^2 - k_y^2)\sigma_x \otimes \tau_z + 2k_x k_y \sigma_y \otimes \tau_z]$ emerges [19], serving as spin-mixing perturbations. More notably, within the eigenspace of the model Hamiltonian in Eq. (1), which is spanned by an orbital doublet com-

TABLE I. Crystallographic point groups that permit orbital doublets with a sign-tunable SOC (both positive and negative).

point groups	doublets	SOC-sign
$C_{3h}, D_{3h}, C_6, C_{6v}, C_{6h}, D_6, D_{6h}$	p_{\pm}, d_{\pm}	+
	$d_{\pm 2}$	-
$C_3, C_{3v}, D_3, D_{3d}, S_6$	$p_{\pm}, e'_{g\pm}$	+
	e'_{\pm}	-

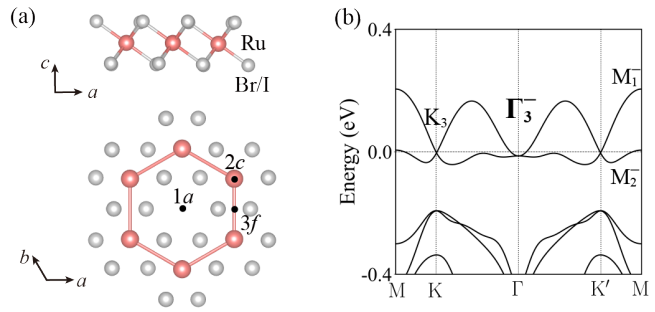


FIG. 3. (a) Crystal structure of RuI_3 and RuBr_3 monolayers with Ru and I/Br atoms represented by red and gray balls, respectively. In the bottom panel, the $1a$, $2c$, and $3f$ maximal Wyckoff positions within the $c = 0$ plane are denoted. (b) Band structures of RuI_3 monolayer without SOC. The Fermi level is set at the zero energy.

bined with electron spin, spin $U(1)$ quasisymmetry is present to eliminate the first-order spin-mixing perturbation [19, 32]. Such a symmetry plays a pivotal role for protecting QSH effects in realistic materials. Consequently, despite a trivial Z_2 index, the ESC systems described by our model can exhibit a near-double-quantized SHC plateau within a sizable bulk gap. In addition, the edge state would open a small gap by spin-mixing perturbation. These features are further confirmed by realistic 2D examples presented in the following section.

II. Realistic materials with tunable SOC

We take the RuI_3 and RuBr_3 monolayers as examples to demonstrate an ESC phase that is accessible through tuning the sign of SOC. The three-dimensional form of RuI_3 has been crystallized in a rhombohedral structure with space group $R\bar{3}$ [33], and its 2D counterpart is in the space group $P\bar{3}1m$, providing the little point group D_{3d} at the Γ point, which is included in Table I. Recent studies have shown that, due to intricate SOC effects combined with strong Ru-I hybridization, RuI_3 exhibits paramagnetic behavior and undergoes a metal-to-insulator transition from bulk to monolayer [33–37]. Therefore, RuI_3 monolayer would be a great platform for investigating SOC effects on topological characteristics. Moreover, RuBr_3 monolayer is also of interest for the variation of the relative importance of the SOC at the Ru and ligand Br/I sites, and for the possibly new topological properties.

We first present the band structures of RuI_3 monolayer in the absence of SOC. Figure 3(b) illustrates that, without SOC, two isolated bands around the Fermi level form crossings at Γ and K points. This band degeneracy is protected by the crystal symmetry and can be lifted by SOC. As shown in Figs. 4 and 5(a), a bulk gap is opened when SOC emerges, signifying the RuI_3 monolayer as a band insulator [individual I and Ru SOC effect in Figs. 4(a) and 4(c), and joint one in Fig. 5(a)]. To characterize the topological phase of RuI_3 monolayer, we calculate

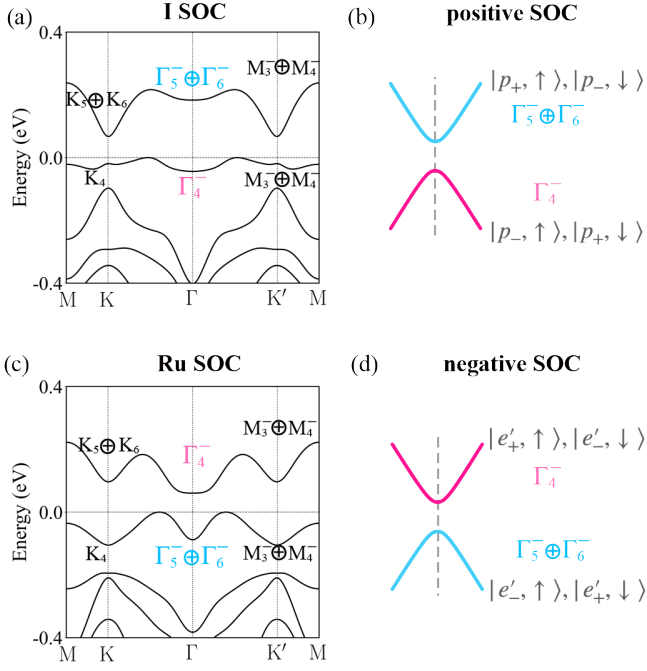


FIG. 4. Band structures of RuI_3 monolayer with (a) only I SOC active and (c) only Ru SOC active. Combined with electron spin, the orbital doublets (b) p_{\pm} of I $5p$ states and (d) e'_{\pm} of Ru $4d-t_{2g}$ states form the co-irreps around the Fermi level at the Γ point, undergoing positive and negative SOC-splitting, respectively.

the Z_2 index by computing the parity eigenvalues of valence bands at two time-reversal-invariant momenta [38], namely Γ and M . The same parity at Γ and M yields a $Z_2 = 0$. As a result, we find that RuI_3 monolayer is a Z_2 trivial insulator.

It is worth to note that within the category of topologically trivial insulators, there exists a special subgroup known as obstructed atomic insulators (OAIs), as proposed based on topological quantum chemistry (TQC) theory [39–43]. Within the TQC framework, for topologically trivial insulators, the band representation (BR) of all occupied bands is a sum of elementary band representations (EBRs) induced from atomic orbitals at maximal Wyckoff positions. And OAI refers to the situation that some of those Wyckoff positions are empty sites without atoms occupied. By calculating the BR of valence bands, we find that the BR decompositions of RuI_3 monolayer have to include an EBR at empty Wyckoff position $1a$, i.e., the center of the honeycomb lattice, see Fig. 3(a). Therefore, RuI_3 monolayer falls into the category of OAIs. This is also captured by the emergence of obstructed metallic edge states, as shown in Fig. 5(c), which appears when one cuts the edge containing the obstructed $1a$ site.

We now take a close look at SOC effects. As shown above, SOC-splitting is responsible for the band gap of RuI_3 monolayer. When we examine the individual contributions of SOC from Ru and I elements, we find that the band splitting in RuI_3 is primarily driven by I SOC, as

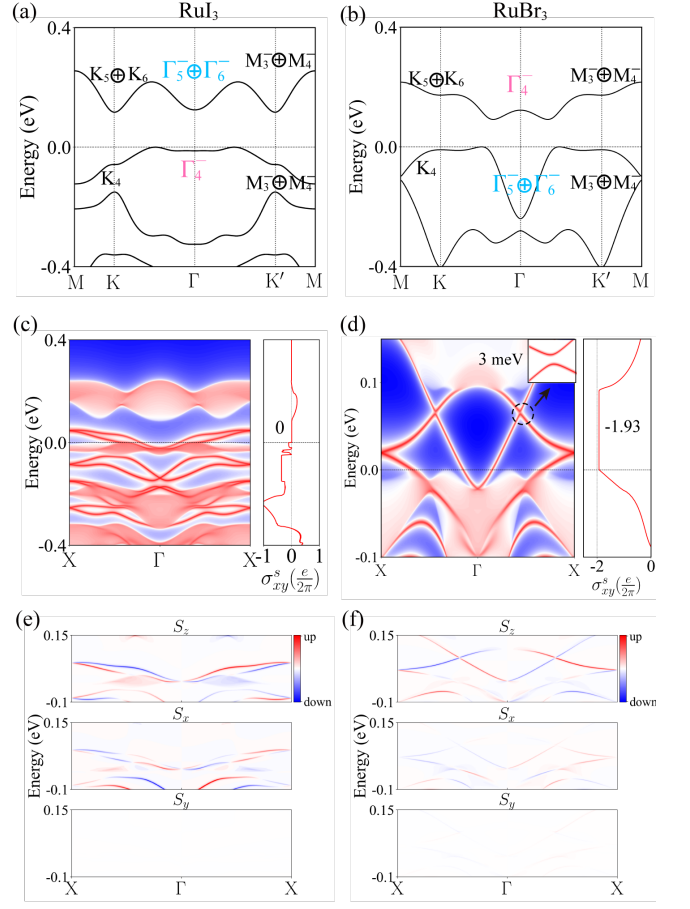


FIG. 5. (a) Band structures with SOC, (c) edge spectrum and SHC, and (e) spin components of the edge states for RuI_3 monolayer; (b), (d), and (f) corresponding results for RuBr_3 monolayer.

evidenced by the same co-irrep feature of the lowest conduction bands and highest valence bands, i.e., $(\Gamma_5^- \oplus \Gamma_6^-)$ -over- Γ_4^- , for both Figs. 4(a) and 5(a). In contrast, when Ru SOC is considered independently, as shown in Fig. 4(c), the band gap at Γ point is inverted, yielding a negative splitting Γ_4^- -over- $(\Gamma_5^- \oplus \Gamma_6^-)$. Such SOC-sign-change behavior is well predicted as the case of D_{3d} in Table I.

Despite the fact that either positive or negative SOC-splitting of the orbital doublet does not change Z_2 , the model Hamiltonian in Eq. (1) predicts that the SOC-sign-change triggers a topological phase transition between the trivial $C_S = 0$ phase and the nontrivial $C_S = -2$ phase. To provide a realistic material candidate for the latter case, we naturally move to RuBr_3 , taking into account the reduced SOC strength associated with Br $4p$ electrons and their weaker hybridization with Ru $4d$ states as compared to I $5p$ electrons. As anticipated, our results show a band inversion from RuI_3 to RuBr_3 , as evidenced by the SOC-induced splitting at Γ shifting from a positive $(\Gamma_5^- \oplus \Gamma_6^-)$ -over- Γ_4^- configuration to a negative Γ_4^- -over- $(\Gamma_5^- \oplus \Gamma_6^-)$ one, see Figs. 5(a) and 5(b).

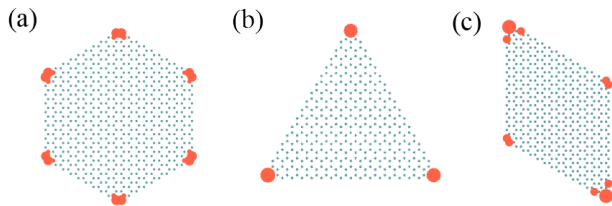


FIG. 6. Spatial distributions of the state at the Fermi level for (a) hexagonal, (b) triangular, and (c) rhomboid-shaped nanodisks of RuBr_3 .

III. Nontrivial features in ESC insulator

Despite both RuI_3 and RuBr_3 belonging to the $Z_2 = 0$ phase, their distinct topological features are evident in the edge and SHC behaviors. In stark contrast to RuI_3 , RuBr_3 exhibits four metallic edge states and two Dirac-like edge crossings, see Figs. 5(c-f). A closer examination of these edge crossings reveals a small gap of 3 meV, which is opened by spin-mixing perturbations. Moreover, unlike the absent SHC in RuI_3 , RuBr_3 exhibits a SHC plateau within a large bulk gap of 130 meV, and the SHC value of -1.93 closely approaches the quantized value of -2 . As discussed above, the transition from RuI_3 to RuBr_3 involves a weakening of the positive SOC from the ligands p orbitals, with the Ru negative SOC become dominant in RuBr_3 , giving rise to the topological phase transition from a trivial insulator with $C_S = 0$ to an ESC insulator with $C_S = -2$. Note that these topologically nontrivial features in RuBr_3 are protected by a nonzero C_S and spin $U(1)$ quasisymmetry [19]. Thus, our findings highlight the orbital-doublet-driven ESC insulators, as described by our nonmagnetic four-band model Hamiltonian, as an ideal platform for realizing QSH effects.

In addition, we note that Ref. [44] has predicted that in ESC insulators, general spin-mixing interactions that open the edge gap introduce a mass term on the edges, accompanied by a phase difference between the mass terms on adjacent edges. Such an edge mass-kink [45] would give rise to corner localized charge and thus the in-gap corner modes, independent of the specific symmetry indicators or the geometry of nanodisks. Here, the ESC insulator RuBr_3 with a spin-mixing induced edge gap closely conforms to the case in Ref. [44]. To check the existence of corner states, we construct nanodisks with hexagonal, triangular, and rhomboid shapes for RuBr_3 and plot the real-space distributions of the state at the Fermi level, which is determined by valence electron counting and resides within the energy range of the edge gap. As shown in Fig. 6, we find that the in-gap states are well localized at the corners, independent of the geometry. Our results are in accordance with theoretical predictions about robust corner states in TRS-preserved $|C_S| = 2$ systems [44]. As a result, manifold nontrivial characteristics embedded in the orbital-doublet-driven ESC insulators, including helical edge states, high near-quantized SHC, and robust in-gap corner modes, enrich their potential applications spanning various fields.

SUMMARY

To summarize, we develop a nonmagnetic four-band model Hamiltonian based on a crystal symmetry-enforced orbital doublet. We propose a generic approach to realize a nontrivial ESC phase with $C_S = -2$ by tuning the sign of SOC within orbital doublets, which can be supported in 12 crystallographic point groups. Realistic 2D examples, specifically the evolution from RuI_3 monolayer to RuBr_3 , demonstrate that a trivial $C_S = 0$ insulator governed by positive SOC transforms into a nontrivial $C_S = -2$ insulator dominated by negative SOC. Moreover, we show that such orbital-doublet-driven ESC insulators manifest nontrivial features, including two pairs of helical edge states, high near-quantized SHC, and robust in-gap corner modes. Our work presents a universal strategy to design ESC insulators featuring a near-double-quantized SHC plateau within a large bulk gap, offering different insights into the exploration of QSH insulators.

ACKNOWLEDGMENTS

Q. L. acknowledges support by National Key R&D Program of China under Grant No. 2020YFA0308900, National Natural Science Foundation of China under Grant No. 12274194, Guangdong Provincial Key Laboratory for Computational Science and Material Design under Grant No. 2019B030301001, Shenzhen Science and Technology Program under Grant No. RCJC20221008092722009, the Science, Technology and Innovation Commission of Shenzhen Municipality under Grant No. ZDSYS20190902092905285 and Center for Computational Science and Engineering of Southern University of Science and Technology. H. W. acknowledges support by the National Natural Science Foundation of China under Grants No. 12174062 and No. 12241402.

Appendix A: Spin Chern number for nonmagnetic four-band model

The low-energy effective Hamiltonian under a D_{6h} point group [Eq. (1)] does not include spin-mixing terms, so we could separate the spin-up and spin-down channels for simplicity. Then the Hamiltonian for the spin-up channel is as follows:

$$H(\mathbf{k}) = \epsilon_0(\mathbf{k})\tau_0 + C[(k_x^2 - k_y^2)\tau_x + 2k_x k_y \tau_y] + [E + D(k_x^2 + k_y^2)]\tau_z \quad (\text{A1})$$

where $\epsilon_0(\mathbf{k}) = A - B(k_x^2 + k_y^2)$. By substituting $k_x = k \cos \phi$ and $k_y = k \sin \phi$, Eq. (A1) can be rewritten as

$$H(\mathbf{k}) = \begin{pmatrix} \epsilon_0(\mathbf{k}) + \cos \theta & \sin \theta e^{-i2\phi} \\ \sin \theta e^{i2\phi} & \epsilon_0(\mathbf{k}) - \cos \theta \end{pmatrix} \quad (\text{A2})$$

where $\cos \theta = \frac{E+Dk^2}{[C^2k^4+(E+Dk^2)^2]^{\frac{1}{2}}}$ and $\sin \theta = \frac{Ck^2}{[C^2k^4+(E+Dk^2)^2]^{\frac{1}{2}}}$. The wave functions are given by

$$|-\rangle = \begin{pmatrix} e^{-i2\phi} \sin \frac{\theta}{2} \\ -\cos \frac{\theta}{2} \end{pmatrix} \quad \text{and} \quad |+\rangle = \begin{pmatrix} e^{-i2\phi} \cos \frac{\theta}{2} \\ \sin \frac{\theta}{2} \end{pmatrix} \quad (\text{A3})$$

with corresponding energies $E_{\pm} = \epsilon_0(\mathbf{k}) \mp \sqrt{C^2k^4 + (E + Dk^2)^2}$. For the lower band $|-\rangle$, the Berry curvature $\Omega_{k\phi}^-$ is

$$\Omega_{k\phi}^- = \Omega_{\theta\phi}^- \frac{\partial(\theta, \phi)}{\partial(k, \phi)} = \left(\frac{\partial A_{\phi}^-}{\partial \theta} - \frac{\partial A_{\theta}^-}{\partial \phi} \right) \frac{\partial(\theta, \phi)}{\partial(k, \phi)} = \frac{2EC^2k^3}{[C^2k^4 + (E + Dk^2)^2]^{3/2}}. \quad (\text{A4})$$

The Chern number of this spin-up band is

$$C_{\uparrow} = \frac{1}{2\pi} \int_0^{\infty} \Omega_{k\phi}^- dk \int_0^{2\pi} d\phi = \text{sgn}(E) - \frac{D}{\sqrt{C^2 + D^2}}. \quad (\text{A5})$$

Therefore, for the continuous model of Eq. (1), the spin Chern number C_S is

$$C_S = \frac{1}{2}(C_{\uparrow} - C_{\downarrow}) = \text{sgn}(E) - \frac{D}{\sqrt{C^2 + D^2}}. \quad (\text{A6})$$

We note that continuous models involving the limit of infinite momentum may yield non-integer and thus non-physical spin Chern numbers. This can be resolved by introducing higher-order k -terms (such as a quadratic correction in the modified Dirac equation) or by mapping the continuous model onto a lattice tight binding model [46, 47]. For the first option, with respecting D_{6h} symmetry operations, we include the k -terms in Eq. (1) up to quartic, $P(k_x^2 + k_y^2)^2 \sigma_z \otimes \tau_z$, and to sextic, $P(k_x^2 + k_y^2)^2 \sigma_z \otimes \tau_z + Q(k_x^2 + k_y^2)^3 \sigma_z \otimes \tau_z$. The derived spin Chern numbers are dependent on the highest order of the k -terms added, with $C_S = \text{sgn}(E) - \text{sgn}(P)$ for the quartic order and $C_S = \text{sgn}(E) - \text{sgn}(Q)$ for the sextic order. One may note that the sign of E consistently contributes to the spin Chern number.

Considering the second approach, i.e., mapping the continuous model to a tight binding model, a four-band Hamiltonian with the p_{\pm} orbitals on a triangular lattice is constructed as

$$\begin{aligned} H(\mathbf{k}) = & \lambda_0 \sigma_z \otimes \tau_z \\ & + 2[\cos(k_y) + 2 \cos(\frac{\sqrt{3}k_x}{2}) \cos(\frac{k_y}{2})] \cdot [(t_{p\sigma 1} + t_{p\pi 1}) \cdot \sigma_0 \otimes \tau_0 + \lambda_1 \cdot \sigma_z \otimes \tau_z] \\ & + 2(t_{p\sigma 1} - t_{p\pi 1}) \cdot [-\cos(k_y) + \cos(\frac{\sqrt{3}k_x}{2}) \cos(\frac{k_y}{2})] \cdot \sigma_0 \otimes \tau_x - 2\sqrt{3}(t_{p\sigma 1} - t_{p\pi 1}) \cdot \sin(\frac{\sqrt{3}k_x}{2}) \sin(\frac{k_y}{2}) \cdot \sigma_0 \otimes \tau_y \\ & + 2[\cos(\sqrt{3}k_x) + 2 \cos(\frac{\sqrt{3}k_x}{2}) \cos(\frac{3k_y}{2})] \cdot [(t_{p\sigma 2} + t_{p\pi 2}) \cdot \sigma_0 \otimes \tau_0 + \lambda_2 \cdot \sigma_z \otimes \tau_z] \\ & + 2(t_{p\sigma 2} - t_{p\pi 2}) \cdot [\cos(\sqrt{3}k_x) - \cos(\frac{\sqrt{3}k_x}{2}) \cos(\frac{3k_y}{2})] \cdot \sigma_0 \otimes \tau_x - 2\sqrt{3}(t_{p\sigma 2} - t_{p\pi 2}) \cdot \sin(\frac{\sqrt{3}k_x}{2}) \sin(\frac{3k_y}{2}) \cdot \sigma_0 \otimes \tau_y \end{aligned} \quad (\text{A7})$$

where the σ and τ represent the Pauli matrices for spin and orbital degrees of freedom, respectively, as in Eq. (1). $t_{p\sigma 1, p\pi 1}$ and $t_{p\sigma 2, p\pi 2}$ represent the first and second-nearest neighbor hopping parameters, respectively. λ_0 denotes the onsite SOC. λ_1 and λ_2 denote the first and second-nearest neighbor SOC, respectively. This lattice model is effectively

mapped to the continuous model in Eq. (1) as $A = 6(t_{p\sigma 1} + t_{p\pi 1} + t_{p\sigma 2} + t_{p\pi 2})$, $B = \frac{3}{2}(t_{p\sigma 1} + t_{p\pi 1} + 3t_{p\sigma 2} + 3t_{p\pi 2})$, $C = \frac{3}{4}(-t_{p\sigma 1} + t_{p\pi 1} - 3t_{p\sigma 2} + 3t_{p\pi 2})$, $D = \frac{3}{2}(-\lambda_1 - 3\lambda_2)$, and $E = \lambda_0 + 6\lambda_1 + 6\lambda_2$. The calculations of the C_S for the valence bands in Eq. (A7) reference the code implemented in the PythTB package [48]. Integration of the Berry curvature is performed using a dense 101×101 k-mesh. We test several sets of λ_0 , λ_1 , and λ_2 , and find that as the sign of E changes from positive to negative, the C_S shifts from 0 to -2 . As a result, the effective Hamiltonian in Eq. (1) serves as a simplified and generalized model, capturing the essential relationship between the sign of E and the topological phase transition.

Appendix B: Band structures of RuF₃ and RuCl₃

See Fig. 7 for the band structures of RuF₃ and RuCl₃.

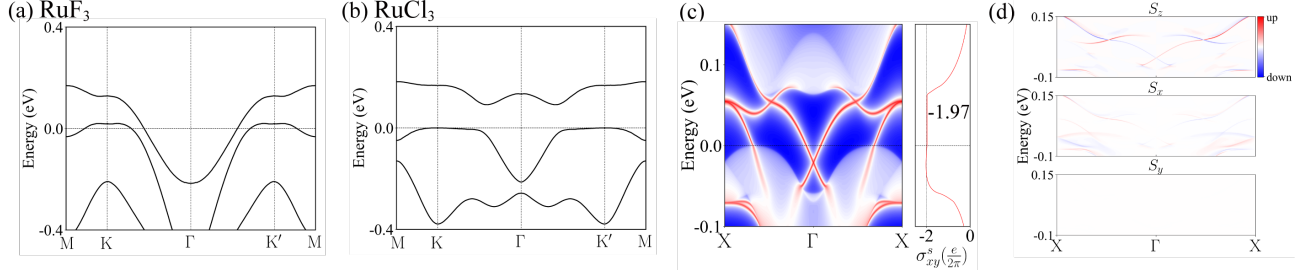


FIG. 7. The band structures of monolayers (a) RuF₃ and (b) RuCl₃ in the nonmagnetic state. The monolayer RuF₃ exhibits metallic behavior, while RuCl₃, similar to RuBr₃ discussed in the main text, is an even spin Chern insulator. As shown in the (c) edge spectrum and SHC and (d) the spin components of edge states, RuCl₃ has two pairs of helical edge states, and its spin Hall conductance plateau within the bulk gap reaches a near-quantized value of -1.97 .

-
- [1] C. L. Kane and E. J. Mele, Quantum spin Hall effect in graphene, *Phys. Rev. Lett.* **95**, 226801 (2005).
 - [2] B. A. Bernevig, T. L. Hughes, and S.-C. Zhang, Quantum spin Hall effect and topological phase transition in HgTe quantum wells, *Science* **314**, 1757 (2006).
 - [3] M. Z. Hasan and C. L. Kane, Colloquium: Topological insulators, *Rev. Mod. Phys.* **82**, 3045 (2010).
 - [4] X.-L. Qi and S.-C. Zhang, Topological insulators and superconductors, *Rev. Mod. Phys.* **83**, 1057 (2011).
 - [5] C. L. Kane and E. J. Mele, Z_2 topological order and the quantum spin Hall effect, *Phys. Rev. Lett.* **95**, 146802 (2005).
 - [6] M. König, S. Wiedmann, C. Brüne, A. Roth, H. Buhmann, L. W. Molenkamp, X.-L. Qi, and S.-C. Zhang, Quantum spin Hall insulator state in HgTe quantum wells, *Science* **318**, 766 (2007).
 - [7] A. Roth, C. Brüne, H. Buhmann, L. W. Molenkamp, J. Maciejko, X.-L. Qi, and S.-C. Zhang, Nonlocal transport in the quantum spin Hall state, *Science* **325**, 294 (2009).
 - [8] I. Knez, R.-R. Du, and G. Sullivan, Evidence for helical edge modes in inverted InAs/GaSb quantum wells, *Phys. Rev. Lett.* **107**, 136603 (2011).
 - [9] S. Tang, C. Zhang, D. Wong, Z. Pedramrazi, H.-Z. Tsai, C. Jia, B. Moritz, M. Claassen, H. Ryu, S. Kahn, J. Jiang, H. Yan, M. Hashimoto, D. Lu, R. G. Moore, C.-C. Hwang, C. Hwang, Z. Hussain, Y. Chen, M. M. Ugeda, Z. Liu, X. Xie, T. P. Devereaux, M. F. Crommie, S.-K. Mo, and Z.-X. Shen, Quantum spin Hall state in monolayer 1T'-WTe₂, *Nature Phys.* **13**, 683 (2017).
 - [10] Z. Fei, T. Palomaki, S. Wu, W. Zhao, X. Cai, B. Sun, P. Nguyen, J. Finney, X. Xu, and D. H. Cobden, Edge conduction in monolayer WTe₂, *Nature Phys.* **13**, 677 (2017).
 - [11] S. Wu, V. Fatemi, Q. D. Gibson, K. Watanabe, T. Taniguchi, R. J. Cava, and P. Jarillo-Herrero, Observation of the quantum spin Hall effect up to 100 Kelvin in a monolayer crystal, *Science* **359**, 76 (2018).
 - [12] F. Reis, G. Li, L. Dudy, M. Bauernfeind, S. Glass, W. Hanke, R. Thomale, J. Schäfer, and R. Claessen, Bismuthene on a SiC substrate: A candidate for a high-temperature quantum spin Hall material, *Science* **357**, 287 (2017).
 - [13] J. L. Collins, A. Tadich, W. Wu, L. C. Gomes, J. N. B. Rodrigues, C. Liu, J. Hellerstedt, H. Ryu, S. Tang, S.-K. Mo, S. Adam, S. A. Yang, M. S. Fuhrer, and M. T. Edmonds, Electric-field-tuned topological phase transition in ultrathin Na₃Bi, *Nature* **564**, 390 (2018).
 - [14] P. Bampoulis, C. Castenmiller, D. J. Klaassen, J. van Mil, Y. Liu, C.-C. Liu, Y. Yao, M. Ezawa, A. N. Rudenko, and H. J. W. Zandvliet, Quantum spin Hall states and topological phase transition in germanene, *Phys. Rev. Lett.* **130**, 196401 (2023).
 - [15] D. N. Sheng, Z. Y. Weng, L. Sheng, and F. D. M. Haldane, Quantum spin-Hall effect and topologically invariant Chern numbers, *Phys. Rev. Lett.* **97**, 036808 (2006).

- [16] K. Kang, Y. Qiu, K. Watanabe, T. Taniguchi, J. Shan, and K. F. Mak, Observation of the double quantum spin Hall phase in moiré WSe₂, [arXiv: 2402.04196](https://arxiv.org/abs/2402.04196) (2024).
- [17] K. Kang, B. Shen, Y. Qiu, Y. Zeng, Z. Xia, K. Watanabe, T. Taniguchi, J. Shan, and K. F. Mak, Evidence of the fractional quantum spin Hall effect in moiré MoTe₂, *Nature* **628**, 522 (2024).
- [18] X.-G. Wen, Symmetry-protected topological phases in noninteracting fermion systems, *Phys. Rev. B* **85**, 085103 (2012).
- [19] L. Liu, Y. Liu, J. Li, H. Wu, and Q. Liu, Quantum spin Hall effect protected by spin $U(1)$ quasi-symmetry, [arXiv:2402.13974](https://arxiv.org/abs/2402.13974) (2024).
- [20] M. Ezawa, High spin-Chern insulators with magnetic order, *Sci. Rep.* **3**, 3435 (2013).
- [21] Y. Bai, L. Cai, N. Mao, R. Li, Y. Dai, B. Huang, and C. Niu, Doubled quantum spin Hall effect with high-spin Chern number in α -antimonene and α -bismuthene, *Phys. Rev. B* **105**, 195142 (2022).
- [22] B. Wang, X. Zhou, Y.-C. Lin, H. Lin, and A. Bansil, High spin-Chern-number insulator in α -antimonene with a hidden topological phase, [arXiv:2202.04162](https://arxiv.org/abs/2202.04162) (2022).
- [23] J. Cook, P.-Y. Yang, T. Volz, C. Connor, R. Satterfield, J. Berglund, Q. Lu, T.-R. Chang, and G. Bian, Engineering a high spin Chern-number insulator in epitaxial Sb monolayer, [arXiv:2312.02316](https://arxiv.org/abs/2312.02316) (2023).
- [24] Y. Xue, W. Xu, B. Zhao, J. Zhang, and Z. Yang, Antiferromagnetic quantum spin Hall insulators with high spin Chern numbers, *Phys. Rev. B* **108**, 075138 (2023).
- [25] P. Blaha, K. Schwarz, F. Tran, R. Laskowski, G. K. H. Madsen, and L. D. Marks, Wien2k: An apw+lo program for calculating the properties of solids, *J. Chem. Phys.* **152**, 074101 (2020).
- [26] V. I. Anisimov, I. V. Solovyev, M. A. Korotin, M. T. Czyżyk, and G. A. Sawatzky, Density-functional theory and NiO photoemission spectra, *Phys. Rev. B* **48**, 16929 (1993).
- [27] J. Kuneš, R. Arita, P. Wissgott, A. Toschi, H. Ikeda, and K. Held, Wien2wannier: From linearized augmented plane waves to maximally localized wannier functions, *Comp. Phys. Commun.* **181**, 1888 (2010).
- [28] A. A. Mostofi, J. R. Yates, Y.-S. Lee, I. Souza, D. Vanderbilt, and N. Marzari, wannier90: A tool for obtaining maximally-localised Wannier functions, *Comput. Phys. Commun.* **178**, 685 (2008).
- [29] Y. Yao and Z. Fang, Sign changes of intrinsic spin Hall effect in semiconductors and simple metals: First-principles calculations, *Phys. Rev. Lett.* **95**, 156601 (2005).
- [30] Q. Wu, S. Zhang, H.-F. Song, M. Troyer, and A. A. Soluyanov, WannierTools: An open-source software package for novel topological materials, *Comput. Phys. Commun.* **224**, 405 (2018).
- [31] D. Dai and M.-H. Whangbo, Analysis of the uniaxial magnetic properties of high-spin d^6 ions at trigonal prism and linear two-coordinate sites: Uniaxial magnetic properties of Ca₃Co₂O₆ and Fe[C(SiMe₃)₃]₂, *Inorg. Chem.* **44**, 4407 (2005).
- [32] J. Li, A. Zhang, Y. Liu, and Q. Liu, Group theory on quasi-symmetry and protected near degeneracy, *Phys. Rev. Lett.* **133**, 026402 (2024).
- [33] D. Ni, X. Gui, K. M. Powderly, and R. J. Cava, Honeycomb-structure RuI₃, a new quantum material related to α -RuCl₃, *Adv. Mater.* **34**, 2106831 (2022).
- [34] K. Nawa, Y. Imai, Y. Yamaji, H. Fujihara, W. Yamada, R. Takahashi, T. Hiraoka, M. Hagihala, S. Torii, T. Aoyama, T. Ohashi, Y. Shimizu, H. Gotou, M. Itoh, K. Ohgushi, and T. J. Sato, Strongly electron-correlated semimetal RuI₃ with a layered honeycomb structure, *J. Phys. Soc. Jpn.* **90**, 123703 (2021).
- [35] D. A. S. Kaib, K. Riedl, A. Razpopov, Y. Li, S. Backes, I. Mazin, and R. Valentí, Electronic and magnetic properties of the RuX₃ (X=Cl, Br, I) family: two siblings—and a cousin?, *npj Quantum Mater.* **7**, 75 (2022).
- [36] Y. Zhang, L.-F. Lin, A. Moreo, and E. Dagotto, Theoretical study of the crystal and electronic properties of α -RuI₃, *Phys. Rev. B* **105**, 085107 (2022).
- [37] L. Liu, K. Yang, G. Wang, D. Lu, Y. Ma, and H. Wu, Contrasting electronic states of RuI₃ and RuCl₃, *Phys. Rev. B* **107**, 165134 (2023).
- [38] L. Fu and C. L. Kane, Topological insulators with inversion symmetry, *Phys. Rev. B* **76**, 045302 (2007).
- [39] B. Bradlyn, L. Elcoro, J. Cano, M. G. Vergniory, Z. Wang, C. Felser, M. I. Aroyo, and B. A. Bernevig, Topological quantum chemistry, *Nature* **547**, 298 (2017).
- [40] J. Cano, B. Bradlyn, Z. Wang, L. Elcoro, M. G. Vergniory, C. Felser, M. I. Aroyo, and B. A. Bernevig, Building blocks of topological quantum chemistry: Elementary band representations, *Phys. Rev. B* **97**, 035139 (2018).
- [41] Y. Xu, L. Elcoro, G. Li, Z.-D. Song, N. Regnault, Q. Yang, Y. Sun, S. Parkin, C. Felser, and B. A. Bernevig, Three-dimensional real space invariants, obstructed atomic insulators and a new principle for active catalytic sites, [arXiv:2111.02433](https://arxiv.org/abs/2111.02433) (2021).
- [42] J. Gao, Y. Qian, H. Jia, Z. Guo, Z. Fang, M. Liu, H. Weng, and Z. Wang, Unconventional materials: the mismatch between electronic charge centers and atomic positions, *Sci. Bull.* **67**, 598 (2022).
- [43] X.-R. Liu, H. Deng, Y. Liu, Z. Yin, C. Chen, Y.-P. Zhu, Y. Yang, Z. Jiang, Z. Liu, M. Ye, D. Shen, J.-X. Yin, K. Wang, Q. Liu, Y. Zhao, and C. Liu, Spectroscopic signature of obstructed surface states in SrIn₂P₂, *Nat. Commun.* **14**, 2905 (2023).
- [44] Y.-C. Hung, B. Wang, A. Bansil, and H. Lin, Time-reversal soliton pairs in even spin-Chern-number higher-order topological insulators, [arXiv:2303.04031](https://arxiv.org/abs/2303.04031) (2023).
- [45] Y.-Q. Wang and J. E. Moore, Boundary edge networks induced by bulk topology, *Phys. Rev. B* **99**, 155102 (2019).
- [46] S.-Q. Shen, W.-Y. Shan, and H.-Z. Lu, Topological insulator and the dirac equation, *Spin* **1**, 33 (2011).
- [47] F. Kirtschig, J. van den Brink, and C. Ortix, Topological classification of k-p hamiltonians for chern insulators, [arXiv:1503.07456](https://arxiv.org/abs/1503.07456) (2015).
- [48] Pythtb website, <https://www.physics.rutgers.edu/pythtb>.